



Rapid calculation of part scale residual stresses in powder bed additive manufacturing

Kajal Khan, L. Srinivasa Mohan, Amitava De & Tarasankar DebRoy

To cite this article: Kajal Khan, L. Srinivasa Mohan, Amitava De & Tarasankar DebRoy (2022): Rapid calculation of part scale residual stresses in powder bed additive manufacturing, Science and Technology of Welding and Joining, DOI: [10.1080/13621718.2022.2139446](https://doi.org/10.1080/13621718.2022.2139446)

To link to this article: <https://doi.org/10.1080/13621718.2022.2139446>

 View supplementary material [↗](#)

 Published online: 31 Oct 2022.

 Submit your article to this journal [↗](#)

 Article views: 25

 View related articles [↗](#)

 View Crossmark data [↗](#)



Rapid calculation of part scale residual stresses in powder bed additive manufacturing

Kajal Khan^{a,b}, L. Srinivasa Mohan^b, Amitava De^{id}^a and Tarasankar DebRoy^c

^aDepartment of Mechanical Engineering, Indian Institute of Technology Bombay, Mumbai, India; ^bAnsys Software Pvt. Ltd., Pune, India;

^cDepartment of Materials Science and Engineering, The Pennsylvania State University, State College, PA, USA

ABSTRACT

Numerical modelling of thermo-mechanical residual stresses for laser powder bed fusion is complex and computationally intensive. A novel analytical model is presented here that can compute the residual stress distributions through a printed part and the baseplate quickly and reliably using phenomenological modelling. The peak residual stress for each deposited layer, needed in the model, is computed using scaling analysis. The computed residual stress distributions are tested with the corresponding independent experimentally measured and numerically computed results. The analytically calculated residual stress distributions are shown to be in good agreement with the corresponding independent results. The analytical model is shown to be 10,000 times faster than the numerical models.

ARTICLE HISTORY

Received 24 May 2022
Revised 13 September 2022
Accepted 19 October 2022

KEYWORDS

Additive manufacturing; laser powder bed fusion; part scale; residual stress distribution; analytical modelling; dimensional analysis

Nomenclature

a_1, b_1, c_1, d_1	coefficients for linear interpolation for 1st layer
a_n, b_n, c_n, d_n	coefficients for linear interpolation for the n th layer
d, d_L	track length, laser spot diameter
E, E_b, E_{pj}	Young's modulus, Young's modulus for the baseplate and j th layer
$e_n, f_n, g_n, q_n, r_n, s_n$	constants in algebraic equations
H	Heaviside step function
H_m	enthalpy at melting
h, h_b	hatch spacing, baseplate height
n	number of layers
P	laser power
Q_b	heat input per unit build volume
Q_v	volumetric heat input
T_a, T_m, T_p	ambient, melting, and preheat temperature
t	layer thickness
v	scanning speed
w, w_b, w_p	width, baseplate width, part width
Y	peak residual stress
β	coefficient of thermal expansion
ΔT	difference between the melting temperature and the preheat temperature
δ	melt pool depth
γ, μ	exponents used for dimensional analysis of peak residual stress
σ_{x1}	longitudinal residual stress

$\sigma_{xnb}, \sigma_{xnt}, \sigma_{xnpj}$	longitudinal residual stresses in the baseplate, transition zone, and j th layer respectively after the deposition of the n th layer
σ_y	material yield stress
$\pi_1, \pi_2, \pi_3, \pi_4, \pi_5$	pi-parameters for dimensional analysis

Introduction

In laser powder bed fusion (LPBF), the solidifying layers experience repeated cycles of heating and cooling resulting in the evolution of thermo-mechanical residual stresses in the finished part [1]. Several researchers [2–8] used numerical models for the estimation of residual stresses in LPBF. These models provided an insight into the evolution of residual stresses but their applications were limited to a few tracks and layers of small dimensions to keep the computational requirements tractable [9,10]. Cheng et al. [7] reported a computational time of around 92 h to calculate residual stresses for LPBF of three 30 μm thick layers of $6 \times 6 \text{ mm}^2$ cross-sectional area. Gibson et al. [11] suggested that a layer-by-layer numerical simulation for LPBF of a part size of $200 \times 200 \times 200 \text{ mm}^3$ with a layer thickness of 20 μm may require up to 89 billion years. An easy-to-use analytical model that can provide a quantitative estimation of the thermo-mechanical residual stress distribution for LPBF in part scale quickly and reliably is, therefore, needed but currently not available.

In contrast to the simulation of layer-by-layer deposition, a lumped layer approach was proposed considering several successive layers together as a single equivalent layer with an imposed strain field [12]. As a result, the lumped layer approach could calculate residual stresses for LPBF of relatively large parts but the redistribution of stresses due to the deposition of individual layers was ignored [12]. A brief description of the previous analytical models to compute the thermo-mechanical residual stresses in LPBF [13–16] is presented in the supplemental documentation. In short, they assumed the imposition of tensile stress, equivalent to the material yield stress, due to the thermal shrinkage of a deposited layer and a linear variation of strain through the part and the baseplate. This approach introduces significant errors since the tensile stress is normally lower than the yield stress.

Here we present an analytical model to compute the distribution of residual stresses in the printed layers and baseplate based on the mechanistic principles of equilibrium of force and moment and consider the peak residual stress as a function of process variables. The analytically computed stress distribution through the thickness of the layers and baseplate is tested against the corresponding available experimentally measured and numerically computed results for LPBF of SS316 powder.

Methodology

Figure 1(a–c) schematically shows the evolution of residual stresses as a molten layer solidifies and cools down to the ambient temperature. The baseplate experiences a temperature gradient and differential thermal strain through its thickness due to the deposited layer. The expansion of the baseplate near its top surface is restricted by the underlying colder material leading to compressive and tensile longitudinal stresses at the top and the bottom, respectively (Figure 1(a)). The solidification and volume shrinkage of the molten layer

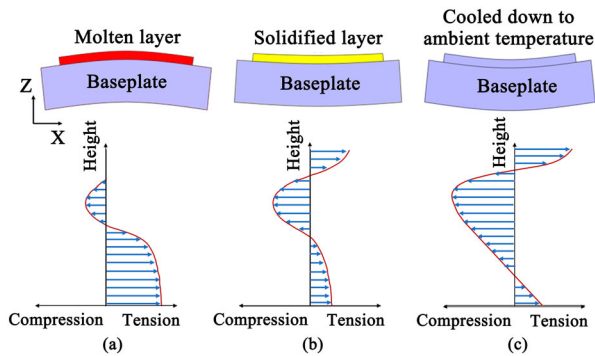


Figure 1. Schematic illustration of the evolution of residual stresses in LPBF during the (a) deposition, (b) solidification, and (c) cooling down of a layer on a baseplate. Height is measured from the bottom of the baseplate.

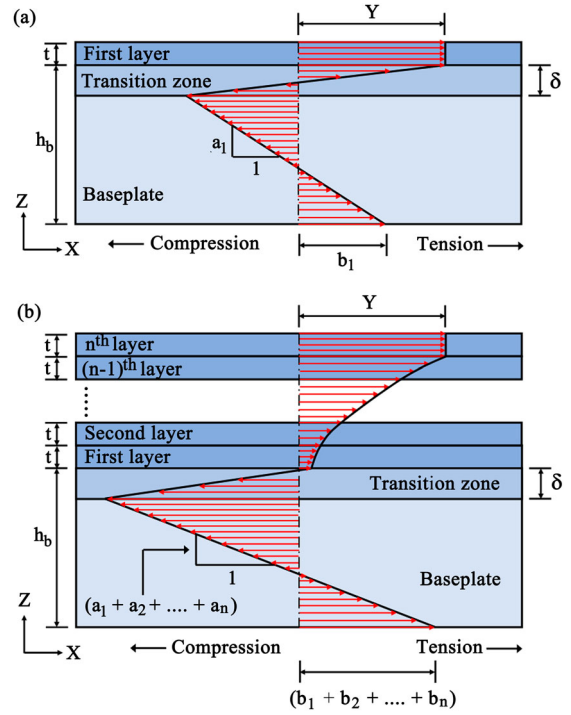


Figure 2. Schematic presentation of residual stress distributions through an assembly consisting of (a) a single-layer, baseplate, and the transition zone, and (b) multiple deposited layers, baseplate, and the transition zone.

is opposed by the baseplate resulting in tensile and compressive stresses in the layer and the baseplate, respectively (Figure 1(b)). The compressive stress in the baseplate accumulates towards the top and annihilates part of the tensile stresses developed earlier at the bottom. As the layer and baseplate cool down to the ambient temperature, the tensile and compressive residual stresses increase in the layer and the baseplate, respectively (Figure 1(c)). The sharp transition of the nature of the stress at the interface between the layer and the baseplate depends on the melt pool depth, layer and baseplate thicknesses, and material properties. Figure 1(c) is illustrated further in Figure 2, which is used to present the proposed analytical model.

Assumptions

The following simplifying assumptions are made to keep the analytical model tractable.

- The material is homogeneous, isotropic, linearly elastic, and exhibits constant properties.
- The longitudinal component of the residual stress is predominant [7] and constant along the width direction. There are no external forces. Further, the layer-wise residual stresses are considered invariant to the edge effect and scanning strategy.

- (c) The melting of each layer is instantaneous. The melt pool depth and peak residual stress are functions of process variables but independent of deposited track and layer numbers.

Analytical modelling

The equilibrium of forces and moments at any cross-section of an assembly of a build part and baseplate can be written following the general beam theory as [17]

$$\int \sigma_{x1}(z)w dz = 0 \quad (1)$$

$$\int \sigma_{x1}(z)wz dz = 0 \quad (2)$$

where σ_{x1} is the longitudinal stress in the x -direction due to the deposition of layer 1, w is the width of the baseplate or layer 1, and $w dz$ is an elemental area on which σ_{x1} is acting. Figure 2(a) shows a schematic nature of the longitudinal stresses through a layer and the baseplate with an intermediate transition region. Considering the longitudinal stress as a continuous function of z through the layer and the baseplate thicknesses, the integrals in Equations (1) and (2) are evaluated separately for the baseplate and the layers. The stresses through the thickness of LPBF deposited individual layers, which are usually around 20 – 100 μm [18], are presumed to be constant [18,19] and expressed as

$$\sigma_{x1p1}(z) = Y \quad (3)$$

where $\sigma_{x1p1}(z)$ is the evolved stress in layer 1 and Y is the peak tensile residual stress. The stress $\sigma_{x1p1}(z)$ is balanced linearly through the baseplate with its top and the bottom experiencing compressive and tensile stresses, respectively. The stress distribution in the baseplate is expressed as

$$\sigma_{x1b}(z) = E_b(a_1z + b_1) \quad (4)$$

where $\sigma_{x1b}(z)$ is the longitudinal stress in the x -direction at any height z measured from the bottom of the baseplate, E_b is Young's modulus of the baseplate material, and a_1 and b_1 are constants. The stress distribution in the transition zone is expressed as

$$\sigma_{x1t}(z) = E_b[c_1\{z - (h_b - \delta)\} + d_1] \quad (5)$$

where $\sigma_{x1t}(z)$ is the longitudinal residual stress in the transition zone, δ is the thickness of the transition zone and assumed to be equal to the depth of the melt pool, h_b is the height of the baseplate, and c_1 and d_1 are constants.

The residual stresses in the solidified layers and the baseplate will accumulate with the deposition of new layers. Following Equations (3–5), the resultant stresses

in the baseplate, the transition zone, and in the n th layer are expressed as,

$$\sigma_{xnb}(z) = E_b \sum_{i=1}^n (a_i z + b_i) \quad (6)$$

$$\sigma_{xnt}(z) = E_b[c_n\{z - (h_b - \delta)\} + d_n] \quad (7)$$

$$\sigma_{xnpn}(z) = Y \quad (8)$$

where $\sigma_{xnb}(z)$, $\sigma_{xnt}(z)$, and $\sigma_{xnpn}(z)$ are the residual stresses, respectively, in the baseplate, transition zone, and the layer n , and a_i , b_i , c_n , and d_n are constants. The stress increment in the baseplate and solidified layers due to the deposition of a new layer is considered as a linear function of z with slope a_i and intercepts b_i . The calculation of the stress increment is done recursively for the deposition of each new layer. Each and every layer in the part experience different stresses due to different stress increment imposed on the solidified layers based on their location and layer number. This leads to a non-linear distribution of stress in the part as a whole. The residual stress in a previously deposited layer j due to the deposition of an upper layer n ($j < n$) is, therefore, expressed as

$$\sigma_{xnpj}(z) = Y + E_{pj} \sum (a_i z + b_i) H\{(i - j)t - \delta\} \text{ for} \\ (j + 1) \leq i \leq n \quad (9)$$

where $\sigma_{xnpj}(z)$ is the residual stress in any layer j after the deposition of the n th layer, E_{pj} is Young's modulus of the j th layer, and t is the layer thickness. In Equation (9), the term $H(i - j)t - \delta$ is a Heaviside function, which is zero for $(i - j)t - \delta < 0$ and, unity for $(i - j)t - \delta \geq 0$. During the deposition of a new layer, the melt pool can penetrate a few underlying solidified layers. The remelting of those underlying layers will nullify the residual stress, which is already developed earlier in those layers. The summation term in the right-hand side of Equation (9) therefore accounts for either cancellation of residual stress in a j th layer due to its remelting or redistribution of residual stress in case there is no remelting of the j th layer during deposition of the upper layers.

Figure 2(b) presents the schematic distribution of residual stresses through the baseplate and multiple layers. The deposition of a new layer results in a peak tensile residual stress (Y) followed by a non-linear stress accumulation through the underlying layers and a linear variation of stresses through the baseplate. A generalised form of Equations (1) and (2) to account for the residual stress distributions through n layers and the baseplate is written as,

$$\int_0^{(h_b - \delta)} \sigma_{xnb} w_b dz + \int_{(h_b - \delta)}^{h_b} \sigma_{xnt} w_b dz + \int_{h_b}^{(h_b + t)} \sigma_{xnp1} w_p dz$$

$$+ \dots + \int_{(h_b+mt)}^{(h_b+nt)} Y w_p dz = 0 \quad (10)$$

$$\begin{aligned} & \int_0^{(h_b-\delta)} \sigma_{xnb} w_b z dz + \int_{(h_b-\delta)}^{h_b} \sigma_{xnt} w_b z dz \\ & + \int_{h_b}^{(h_b+t)} \sigma_{xnp1} w_p z dz + \dots + \int_{(h_b+mt)}^{(h_b+nt)} Y w_p z dz \\ & = 0 \end{aligned} \quad (11)$$

where $m = (n - 1)$, and σ_{xnp1} is the residual stress in the first layer adjoining the baseplate. In Equation (10), the first and the second terms account for the forces in the baseplate and the transition zone, respectively. The last term in Equation (10) represents the force in the topmost layer due to a peak tensile residual stress (Y), and the intermediate terms estimate the forces in the deposited layers below the topmost one. Likewise, Equation (11) accounts for the calculation of moments from the baseplate to the topmost layer. The distributions of residual stresses are computed recursively by solving Equations (10) and (11) with the stresses in the baseplate, transition zone, and deposited layers expressed as Equations (6–9). This is contemplated by expressing c_n and d_n in Equation (7) in terms of a_n and b_n as the first step,

$$c_n = \frac{1}{\delta} \left[\frac{Y}{E_b} - d_n + \frac{E_{p1}}{E_b} \sum_{i=2}^n (a_i h_b + b_i) H\{(i-1)t - \delta\} \right] \quad (12)$$

$$d_n = \sum_{i=1}^n \{a_i (h_b - \delta) + b_i\} \quad (13)$$

Next, Equations (10) and (11) are expressed in the corresponding algebraic forms as

$$a_n e_n + b_n f_n = g_n \quad (14)$$

$$a_n q_n + b_n r_n = s_n \quad (15)$$

where the constants $e_n, f_n, g_n, q_n, r_n, s_n$ are given in Appendix. For every new layer deposited, the terms a_n and b_n are solved iteratively to find out the overall distribution of residual stresses. Based on the values of a_n and b_n , the residual stress calculated using Equation (9) in each layer of the part can be either tensile or compressive in nature. A prior estimation of the melt pool depth (δ) and the peak tensile residual stress (Y) for the deposition of a new layer is required to calculate the residual stress distributions using Equations (10) and (11). The scaling analysis for the melt pool depth (δ) follows a previous work [20] and is presented in the supplementary document. The scaling analysis to estimate

the peak tensile residual stress (Y) is presented in the following section.

Estimation of peak residual stress (Y)

The scaling analysis for the estimation of the peak tensile residual stress (Y) in a deposited layer is undertaken using the Buckingham π -theorem. Table 1 shows the list of five variables that are considered to affect the residual stress with their units and dimensions in the MLT system. The parameter Q_b is the heat input per unit build volume and is estimated as $P/(\nu ht)$, where P, ν, h , and t refer to the laser power, scanning speed, hatch spacing, and layer thickness, respectively [21]. The ratio Q_b/H_m is referred to as the dimensionless heat input per unit build volume where H_m is the enthalpy at melting. The variable $\beta \Delta T$ denotes the thermal strain where β is the coefficient of thermal expansion or contraction and ΔT is the difference between the melting temperature and the preheat temperature. The other parameters in Table 1 include the dimensionless preheat temperature (T_p/T_a), laser spot diameter (d_L), and the deposited track length (d) for a layer. The peak tensile residual stress (Y) is considered in a dimensionless form as Y/σ_y , where σ_y is the yield strength of the powder alloy.

Considering one fundamental dimension L and a total of six variables as shown in Table 1, five ($6 - 1 = 5$) π terms ($\pi_1, \pi_2, \pi_3, \pi_4$, and π_5) are formed as

$$\pi_1 = \frac{Y}{\sigma_y}; \quad (16)$$

$$\pi_2 = \frac{Q_b}{H_m}; \quad (17)$$

$$\pi_3 = \beta \Delta T; \quad (18)$$

$$\pi_4 = \frac{T_p}{T_a}; \quad (19)$$

$$\pi_5 = d_L^\gamma d^\mu \quad (20)$$

Applying Buckingham π -theorem to solve for the powers γ and μ , the term π_5 is obtained as

$$\pi_5 = \frac{d}{d_L} \quad (21)$$

The influence of the variables in Table 1 on the peak residual stress (Y) in a deposited layer is examined

Table 1. Parameters used for dimensional analysis of residual stress (Y).

Parameters	Symbol	Unit	Dimension
Dimensionless heat input per unit build volume	Q_b/H_m	–	–
Thermal strain	$\beta \Delta T$	–	–
Dimensionless preheat temperature	T_p/T_a	–	–
Laser spot diameter	d_L	m	L
Track length	d	m	L
Dimensionless peak residual stress	Y/σ_y	–	–

to find a suitable relation among π_1 , π_2 , π_3 , π_4 , and π_5 . An increase in the heat input per unit build volume (Q_b) results in a greater provision of heat, higher peak temperature, and greater residual stress [22]. An increase in the thermal strain ($\beta\Delta T$) enhances the residual stress [23]. A higher value of preheat temperature would reduce the temperature gradient and the resulting residual stress and thus, an inverse relationship exists between π_1 and π_4 . For a longer track, the heat accumulation and temperature gradient (ΔT) will increase resulting in an increase in the peak residual stress [7,24]. A material with a higher yield strength (σ_y) will pose a greater resistance to thermal strain and result in higher peak residual stress [22]. The dimensionless peak residual stress π_1 is therefore influenced directly by the terms π_2 , π_3 , and π_5 , and inversely by π_4 . A set of 25 experimentally measured peak residual stresses from independent literature for LPBF of SS316 and the corresponding process conditions [25] is used next to find the best fit functional relation for π_1 as a function of π_2 , π_3 , π_4 , and π_5 , which is expressed in an explicit form as

$$\frac{Y}{\sigma_Y} = 0.32 \left[\frac{(Q_b/H_m) (\beta\Delta T) (\sqrt{d/d_L})}{(T_p/T_a)} \right]^{0.77} \quad (22)$$

Figure 3 shows the experimentally measured peak residual stresses from the literature [25] in the form of (Y/σ_Y) , and the best fit line with the correlation coefficient (R^2) as 0.91. The parameter on the right-hand side in Equation (22) is a product of four dimensionless variables and depicts a scaling factor to calculate the residual stress of a layer in terms of the yield stress of SS316 powder for a given LPBF condition. The estimated peak tensile residual stress (Y) from Equation (22) is used as input to Equations (10) and (11) to calculate the stress distribution through the printed layers and the baseplate for an LPBF condition.

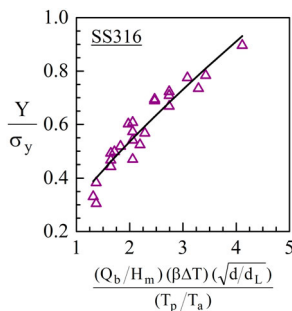


Figure 3. Dimensionless peak residual stress as a function of four dimensionless variables for LPBF of SS316 powder. The best fit line (in black) is plotted following the least square method [25].

Model testing and validation

Residual stress distribution in a single-layer deposit

The analytical model is tested first to calculate the residual stress distributions for LPBF of a single-layer SS316 deposit onto a baseplate, for which numerically computed residual stresses and distortions, and a comparison of the computed and corresponding measured distortions are reported in the literature [19]. Since the part distortion is an outcome of evolved residual stresses through the part and the baseplate and the combined stiffness of the assembly, the numerically computed residual stresses in reference [19] are considered rational for a comparison with the analytically computed stresses.

Figure 4(a) shows the cross-section of the baseplate and the deposited layer with a blue dashed line along which the residual stress distribution is computed using the finite element method [19]. Figure 4(b) shows the numerically computed [19] and the corresponding analytically calculated residual stress distributions. For the given condition, the melt pool depth (δ) and the peak residual stress (Y) for the deposited layer are estimated as 209 μm and 303 MPa and used as input for the analytical model calculations.

Figure 4(b) shows that the stress is tensile and constant in the deposited layer, transitions to compressive through the layer-baseplate interface and changes to tensile towards the bottom of the baseplate. The analytically computed values of the peak compressive and tensile stresses are around 215 and 153 MPa, respectively. The numerically calculated stress distributions show a similar pattern with the peak tensile stress of 380 MPa in the layer, the maximum compressive and tensile stresses of around 173 and 76 MPa, respectively, at the layer-baseplate interface and bottom of the baseplate [19]. An overall difference of around 25% is observed between the analytically calculated and the corresponding numerically computed residual stress distribution.

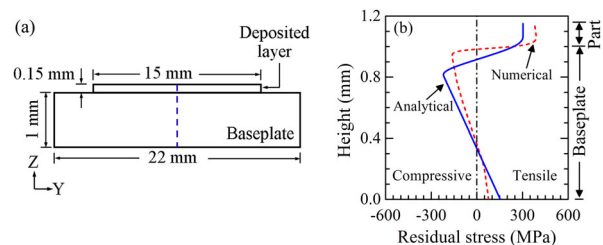


Figure 4. (a) Schematic of a single-layer deposit cross-section of SS316 powder on a baseplate [LPBF conditions: laser power = 300 W, laser spot diameter = 600 μm , scanning velocity = 50 mm s^{-1} , layer thickness = 150 μm , track length = 3 mm, hatch spacing = 100 μm] [19]. (b) Comparison of numerically computed [19] and corresponding analytically calculated longitudinal residual stress distribution along the blue dashed line.

The difference is partly due to the errors in the estimation of the melt pool depth (δ) and peak residual stress (Y) following the scaling analyses as well as the assumptions in the numerical model calculations [19]. A similar order of residual stress and its nature of transition from tensile to compressive through the printed layers and layer-baseplate interface are also reported in the literature for LPBF of SS316 [8,26].

Residual stress distribution in a 100-layer deposit

The analytical model is used next to compute the residual stress distributions for LPBF of a 100-layer SS316 deposit of 5 mm height using the process conditions from the literature [27]. The authors in reference [27] have used a two-dimensional finite element method-based numerical model with lumping of multiple layers into equivalent ones to compute the stresses. Figure 5(a) shows the cross-section of the baseplate and the deposit with a blue dashed line along which the stresses are computed. The melt pool depth (δ) and the peak residual stress (Y) are estimated respectively as $72 \mu\text{m}$ and 423 MPa and used as input for the analytical model calculations. The evolution of the stresses is computed recursively for the deposition of each new layer following Equations (6–11) and shown in Figure 5(b). The analytically calculated stress distributions through the layers show very little variations, from 423 MPa to around 395 MPa, which is attributed to a smaller number of layers. The numerically calculated stresses through the layers also show a nearly constant value of around 528 MPa (Figure 5(b)). The analytically calculated stresses show a sharp transition through the part-baseplate interface, which can lead to cracking and premature separation of the part from the baseplate [28]. The analytical calculations show further a linear stress distribution through the baseplate with a tensile stress of around 16 MPa at the bottom of the baseplate.

The analytical model is used further to calculate the residual stress distributions considering a 1000-layer deposit of 50 mm height using the same process conditions to illustrate how a non-linear nature of stresses can evolve with increasing layer numbers. Figure 5(c) presents the cross-section of the baseplate and the deposited layers. Figure 5(d) shows a non-linear nature of the analytically calculated stresses through the deposited layers that vary from 423 MPa at the topmost layer to 18 MPa at a height of 15 mm, which increases again to 169 MPa near the bottommost layer. A sharp transition of the stresses from tensile to compressive occurs through the part-baseplate interface followed by a linear variation of stresses from compressive to tensile with a tensile stress of around 216 MPa at the bottom of the baseplate. Figure 5(d) shows that the analytical model is capable of calculating layer-by-layer evolutions of residual stress distributions through a printed

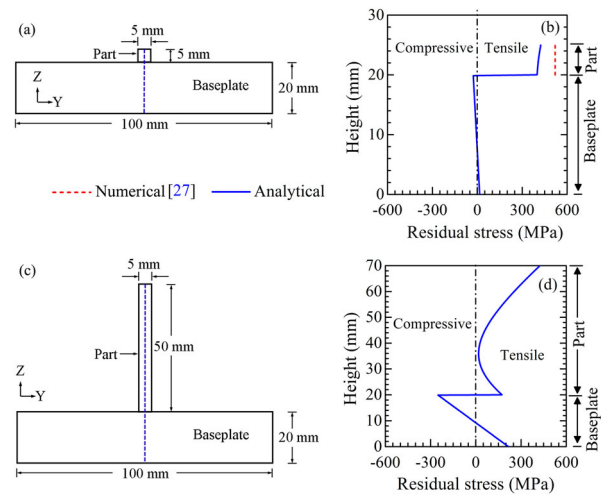


Figure 5. (a) Schematic of a 100-layer SS316 deposit on a baseplate [LPBF conditions: laser power = 370 W, laser spot diameter = $100 \mu\text{m}$, scanning velocity = 800 mm s^{-1} , layer thickness = $50 \mu\text{m}$, hatch spacing = $100 \mu\text{m}$] [27], (b) Comparison of numerically computed [27] and corresponding analytically calculated longitudinal residual stress distribution through the 100 layer deposit and baseplate thickness, (c) Schematic of a 1000-layer SS316 deposit on a baseplate considering the same conditions as above, (d) Analytically calculated residual stress distribution through the 1000 layer deposit and baseplate thickness.

part of several hundreds of layers, which is deemed intractable by standard numerical models.

Residual stress distribution in a 200-layer deposit

The analytically calculated residual stresses are further validated against the corresponding experimentally measured and numerically computed results for LPBF of a 200-layer SS316 part on a baseplate as shown in Figure 6(a) and reported in the literature [29]. The baseplate in reference [29] exhibits a central hole. The baseplate height is therefore reduced by half in the analytical calculations for an approximate compensation of the baseplate stiffness. The residual stress distribution is considered along the blue dashed line in Figure 6(a) and compared with the corresponding experimentally measured [29] and numerically computed results [29] in Figure 6(b). The neutron diffraction method is used to measure the residual stresses between 1.75 and 8.25 mm from the part bottom [29]. The melt pool depth (δ) and the peak residual stress (Y) are estimated as $152 \mu\text{m}$ and 415 MPa, respectively, and used as input for the analytical model calculations.

The analytically calculated residual stress distribution through the part shows a non-linear nature similar to that reported by experimental measurements [29] and numerical model calculations [29]. The measured stress at 1.75 mm below the top surface is around 200 MPa [29] and the corresponding numerically computed [29] and analytically calculated stresses are 250 and 275 MPa, respectively. At a height of 4 mm from

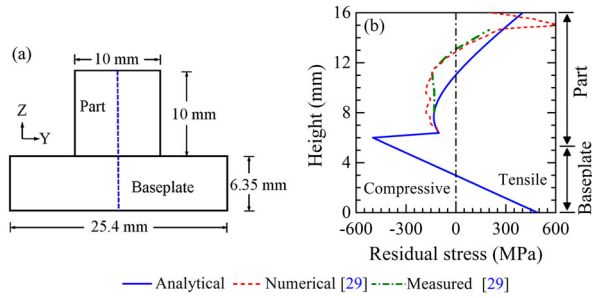


Figure 6. (a) Schematic cross-section of a 200-layer deposit of SS316 powder on a baseplate [LPBF conditions: laser power = 250 W, laser spot diameter = 80 μm , scanning velocity = 278 mm s^{-1} , layer thickness = 50 μm , track length = 5 mm, hatch spacing = 100 μm] [29]. (b) Comparison of analytically calculated and corresponding experimentally measured [29], and numerically computed [29] longitudinal residual stress distribution along the blue dashed line in Figure 6(a).

the part bottom, the experimentally measured residual stress is compressive and around 135 MPa [29]. The corresponding numerically computed [29] and analytically calculated stresses are also compressive and around 175 and 40 MPa, respectively. At a location 1.75 mm above the part bottom, the measured residual stress remains compressive and is around 130 MPa [29]. The corresponding numerically computed [29] and analytically calculated stress also remain compressive and equal to around 178 and 129 MPa, respectively. The analytical calculations show further a sharp rise of the compressive stress to around 499 MPa followed by a transition to a tensile stress of around 491 MPa through the part-baseplate interface to the bottom of the baseplate. Overall, the analytically computed residual stress distributions show a good agreement with the corresponding experimentally measured [29] and numerically computed [29] results except at the centre height of the part.

Computational time

Table 2 shows the model details, the hardware used, and the execution run-times for the typical thermo-mechanical analysis for LPBF of a single and multiple layers using the finite element method [19,27,29]. The calculations for the analytical model are performed with an 11th-generation core i5 notebook computer with 8 GB RAM and 4.2 GHz hardware speed and the

corresponding computational times are also presented in Table 2.

Table 2 shows that the analytical model is nearly 10^4 times faster than the numerical models. The analytical model can consider the effect of the layer-by-layer deposition of powder alloys including the variation of the geometric cross-sections. The analytically computed results of the residual stress distribution following the mechanistic principles of the equilibrium of forces and moments show a good accuracy, which establishes its usefulness as a practical tool for the estimation of residual stress distribution for LPBF.

Summary and conclusions

A novel analytical framework is presented and tested against independent numerical and experimental observations for the calculation of longitudinal residual stress distribution for LPBF of SS316 alloy. The analytical model follows the mechanistic principles of equilibrium of forces and moments to calculate the distribution of residual stresses through the deposited layers and the baseplate. Two unique routes are presented for the scaling analysis of the melt pool depth and the peak tensile residual stress for the deposition of a layer, which are used in the analytical model for the calculation of residual stress distribution.

The proposed analytical model is further demonstrated to be computationally efficient as it can provide the calculated residual stress distributions nearly 10^4 times faster than the numerical models. Currently, the application of numerical models, which calculate the layer-by-layer distribution of residual stresses, is not available for LPBF in part scale. The proposed model can be used as a practical tool to get an overall estimation of the residual stress distribution without the need for complex calculations and expensive computers.

Based on the present work, the following points are concluded.

- (1) A direct analytical estimation of the residual stress distributions through the deposited layers and the baseplate following the mechanistic principles of equilibrium of forces and moments is a viable option for LPBF in part scale. The proposed analytical model is unique and provides the distributions

Table 2. Execution times to compute residual stress distributions for LPBF of single and multi-layer builds using numerical models [19,27,29] and proposed analytical model.

Dimension (mm^3)	Simulation details				Single-core equivalent run time (h)	
	Computed layers	Nodes	Elements	Hardware speed	Numerical	Analytical
$35 \times 15 \times 0.15$	1	111,908	63820	4.2 GHz	~ 8.4 [19]	0.0003
$50 \times 5 \times 50$	100	495,504	494010		$\sim 29.4^{\text{a}}$ [27]	0.0833
$20 \times 10 \times 10$	200	344,750	329250		$\sim 9280^{\text{b}}$ [29]	0.0150

^aEstimated based on 2-D plane stress finite element simulation.

^bEstimated based on element count and number of layers.

of residual stresses for LPBF of all size deposits with fair accuracy.

- (2) The melt pool depth and the peak tensile residual stress for the deposition of a layer are estimated by using scaling analysis and provided as input to the analytical model. These are developed using simple dimensional analysis and a fairly large volume of data from the literature for a wide range of process conditions in laser powder bed fusion of SS316.
- (3) The analytically calculated residual stress distributions are in good agreement with the corresponding reported numerically computed and experimentally measured results.
- (4) The analytical model can calculate the distributions of residual stresses for laser powder bed fusion much faster than the available numerical models. For example, the residual stress distribution for laser powder bed fusion of a build volume of 78 mm³ can be analysed in about one second using a core i5 notebook computer with 8GB RAM.

Disclosure statement

No potential conflict of interest was reported by the author(s).

Data availability statement

The raw/processed data required to reproduce these findings cannot be shared at this time due to technical or time limitations.

ORCID

Amitava De  <http://orcid.org/0000-0002-3109-261X>

References

- [1] DebRoy T, Mukherjee T, Wei HL, et al. Metallurgy, mechanistic models and machine learning in metal printing. *Nat Rev Mater*. 2021;6(1):48–68.
- [2] Xiao Z, Chen C, Zhu H, et al. Study of residual stress in selective laser melting of Ti6Al4V. *Mater Des*. 2020;193:108846.
- [3] Marques BM, Andrade CM, Neto DM, et al. Numerical analysis of residual stresses in parts produced by selective laser melting process. *Procedia Manuf*. 2020;47:1170–1177.
- [4] Gu D, He B. Finite element simulation and experimental investigation of residual stresses in selective laser melted Ti-Ni shape memory alloy. *Comput Mater Sci*. 2016;117:221–232.
- [5] Dai K, Shaw L. Thermal and stress modeling of multi-material laser processing. *Acta Mater*. 2001;49(20):4171–4181.
- [6] Li Y, Zhou K, Tan P, et al. Modeling temperature and residual stress fields in selective laser melting. *Int J Mech Sci*. 2018;136:24–35.
- [7] Cheng B, Shrestha S, Chou K. Stress and deformation evaluations of scanning strategy effect in selective laser melting. *Addit Manuf*. 2016;12:240–251.
- [8] Bian P, Shi J, Shao X, et al. Evolution of cyclic thermal stress in selective laser melting of 316L stainless steel: A realistic numerical study with experimental verification. *Int J Adv Manuf Technol*. 2019;104(9-12):3867–3882.
- [9] Khan K, De A. Modelling of selective laser melting process with adaptive remeshing. *Sci Technol Weld Join*. 2019;24(5):391–400. doi:10.1080/13621718.2019.1575057.
- [10] Megahed M, Mindt HW, N'Dri N, et al. Metal additive-manufacturing process and residual stress modeling. *Integr Mater Manuf Innov*. 2016;5(1):1–33.
- [11] Gibson I, Rosen D, Stucker B, Khorasani M. Additive manufacturing technologies, 3rd ed. Cham: Springer; 2021.
- [12] Malmelöv A, Lundbäck A, Lindgren LE. History reduction by lumping for time-efficient simulation of additive manufacturing. *Metals (Basel)*. 2020;10(1):58.
- [13] Shiomi M, Osakada K, Nakamura K, et al. Residual stress within metallic model made by selective laser melting process. *CIRP Ann-Manuf Technol*. 2004;53(1):195–198.
- [14] Mercelis P, Kruth JP. Residual stresses in selective laser sintering and selective laser melting. *Rapid Prototyp J*. 2006;12(5):254–265.
- [15] Boruah D, Zhang X, Doré M. An analytical method for predicting residual stress distribution in selective laser melted/sintered alloys. *Mater Res*. 2018;6:283–288.
- [16] Chahal V, Taylor RM. Model development for residual stress consideration in design for laser metal 3D printing of maraging steel 300. In: Proc. 29th SFF Symp., Austin, TX, USA; 2018. p. 623–634.
- [17] Timoshenko S. Strength of materials – part 1. 2nd ed. London (UK): D Van Nostrand Co Inc; 1940.
- [18] Liu S, Shin YC. Additive manufacturing of Ti6Al4V alloy: a review. *Mater Des*. 2018;164:8–12.
- [19] Li C, Liu JF, Guo YB. Prediction of residual stress and part distortion in selective laser melting. *Procedia CIRP*. 2016;45:171–174.
- [20] Khan K, Mohr G, Hilgenberg K, et al. Probing a novel heat source model and adaptive remeshing technique to simulate laser powder bed fusion with experimental validation. *Comput Mater Sci*. 2020;181:109752.
- [21] Simson T, Emmel A, Dwars A, et al. Residual stress measurements on AISI 316L samples manufactured by selective laser melting. *Addit Manuf*. 2017;17:183–189.
- [22] Wu Q, Mukherjee T, De A, et al. Residual stresses in wire-arc additive manufacturing—hierarchy of influential variables. *Addit Manuf*. 2020;35:101355.
- [23] Vrancken B. Study of residual stresses in selective laser melting [Thesis]. Leuven: KU Leuven Faculty of Engineering Science; 2016.
- [24] Liu Y, Yang Y, Wang D. A study on the residual stress during selective laser melting (SLM) of metallic powder. *Int J Adv Manuf Technol*. 2016;87(1-4):647–656.
- [25] Yakout M, Elbestawi MA, Veldhuis SC. Density and mechanical properties in selective laser melting of Invar 36 and stainless steel 316L. *J Mater Process Technol*. 2019;266:397–420.
- [26] Hodge NE, Ferencz RM, Vignes RM. Experimental comparison of residual stresses for a thermomechanical model for the simulation of selective laser melting. *Addit Manuf*. 2016;12:159–168. doi:10.1016/j.addma.2016.05.011.
- [27] Kim T, Ha K, Cho YR, et al. Analysis of residual stress evolution during powder bed fusion process of AISI 316L stainless steel with experiment and numerical modeling. *Int J Adv Manuf Technol*. 2019;105(1-4):309–323.
- [28] Mukherjee T, Zhang W, DebRoy T. An improved prediction of the residual stresses and distortion in additive manufacturing. *Comput Mater Sci*. 2017;126:360–272.

[29] Smith WL, Roehling JD, Strantz M, et al. Residual stress analysis of in situ surface layer heating effects on laser powder bed fusion of 316L stainless steel. *Addit Manuf.* 2021;47:102052.

Appendix

Evaluations of coefficients for Equations (14) and (15)

The integrals in Equations (10) and (11) are evaluated after obtaining the stresses from Equations (6–9) and writing the coefficients c_n and d_n in terms of the coefficients a_n and b_n using Equations (12) and (13). Equations (10) and (11) are finally rearranged into two algebraic equations in terms of the coefficients a_n and b_n as given in Equations (14) and (15). The coefficients in Equations (14) and (15) are $e_n, f_n, g_n, q_n, r_n, s_n$ and given as

$$e_n = h_b(h_b - \delta) + \frac{E_{p1}}{E_b} h_b \delta H(mt - \delta) + \frac{w_p t}{w_b} \sum_{i=1}^m \frac{E_{pi}}{E_b} \{[2h_b + (2i - 1)t] H\{(n - i)t - \delta\}\} \quad (A1)$$

$$f_n = (2h_b - \delta) + \frac{E_{p1}}{E_b} \delta H(mt - \delta) + \frac{2w_p t}{w_b} \sum_{i=1}^m \frac{E_{pi}}{E_b} H\{(n - i)t - \delta\} \quad (A2)$$

$$g_n = -\frac{Y}{E_b} \frac{2w_p t}{w_b} \quad (A3)$$

$$q_n = (2h_b^3 - 3h_b^2\delta + h_b\delta^2) + \frac{E_{p1}}{E_b} \{h_b\delta(3h_b - \delta)\} H(mt - \delta) + \frac{2w_p}{w_b} \sum_{i=1}^m \frac{E_{pi}}{E_b} \{[(h_b + it)^3 - (h_b + (i - 1)t)^3]\} H\{(n - i)t - \delta\} \quad (A4)$$

$$r_n = (3h_b^2 - 3h_b\delta + \delta^2) + \frac{E_{p1}}{E_b} \{\delta(3h_b - \delta)\} H(mt - \delta) + \frac{3w_p}{w_b} \sum_{i=1}^m \frac{E_{pi}}{E_b} \{[(h_b + it)^2 - (h_b + (i - 1)t)^2]\} H\{(n - i)t - \delta\} \quad (A5)$$

$$s_n = -\frac{Y}{E_b} \left[\frac{3w_p t}{w_b} \{2h_b + (2n - 1)t\} \right] \quad (A6)$$

where $m = (n - 1)$.